

# Airborne spectral radiation measurements to derive solar radiative forcing of Saharan dust mixed with biomass burning smoke particles

By S. BAUER<sup>1\*</sup>, E. BIERWIRTH<sup>1</sup>, M. ESSELBORN<sup>2†</sup>, A. PETZOLD<sup>2</sup>, A. MACKE<sup>3</sup>, T. TRAUTMANN<sup>2</sup> and M. WENDISCH<sup>1</sup>, <sup>1</sup>Leipzig Institute for Meteorology (LIM), University of Leipzig, Stephanstr. 3, 04103 Leipzig, Germany; <sup>2</sup>Deutsches Zentrum für Luft- und Raumfahrt (DLR), Oberpfaffenhofen, Germany; <sup>3</sup>Leibniz Institute for Tropospheric Research (IfT), Germany

(Manuscript received 20 December 2010; in final form 6 June 2011)

## ABSTRACT

Airborne measurements of upward solar spectral irradiances were performed during the second Saharan Mineral dUst experiMent (SAMUM-2) campaign based on the Cape Verde Islands. Additionally, airborne high resolution lidar measurements of vertical profiles of particle extinction coefficients were collected in parallel to the radiation data. Aerosol layers of Saharan dust, partly mixed with biomass-burning smoke, were probed. With corresponding radiative transfer simulations the single scattering albedo and the asymmetry parameter of the aerosol particles were derived although with high uncertainty. The broad-band aerosol solar radiative forcing at the top of atmosphere was calculated and examined as a function of the aerosol types. However, due to uncertainties in both the measurements and the calculations the chemical composition cannot be identified. In addition, a mostly measurement-based method to derive the broad-band aerosol solar radiative forcing was used. This approach revealed clear differences of broad-band net irradiances as a function of the aerosol optical depth. The data were used to identify different aerosol types from different origins. Higher portions of biomass-burning smoke lead to larger broad-band net irradiances.

## 1. Introduction

Airborne Saharan dust is one of the important atmospheric aerosol components determining the radiation budget of the atmosphere. The Intergovernmental Panel on Climate Change (IPCC, 2007) specifies the global direct radiative effect of aerosol particles in the atmosphere with a radiative forcing of  $-0.5 \text{ W m}^{-2}$ , and an uncertainty of  $0.4 \text{ W m}^{-2}$  (Forster et al., 2007). Solar radiation is partly absorbed by Saharan dust particles, which leads to local warming of the atmosphere. It is also scattered which results in a cooling beneath the dust layer. Studies about the impact of aerosol optical properties such as single scattering albedo, asymmetry parameter and aerosol optical depth on the radiative forcing of Saharan dust and biomass-burning smoke were published by Wang et al. (2007) and Shell and Somerville (2007). Experiments like NAMMA (Chen et al., 2010), SHADE (Tanre et al., 2003), DODO (Formenti et al.,

2008) or on Lampedusa Island (Meloni et al., 2006) focused on the chemical composition of mineral dust and their radiative properties. Analysis of mixings of mineral dust and biomass-burning smoke with respect to their impact on radiative forcing were performed in Granada, Spain (Lyamani et al., 2006) and for the experiment DABEX (Johnson et al., 2009).

By considering the net irradiances in the solar and terrestrial wavelength ranges, the cooling and warming effects of dust aerosols can be quantified. During the first Saharan Mineral dUst experiMent (SAMUM-1) in Morocco 2006 near the Saharan source region (Heintzenberg, 2009) it was shown that the solar aerosol radiative forcing at the top of atmosphere (TOA) over land was positive (warming) for broad-band solar surface albedos larger than 0.3 and negative for albedos less than 0.3 (cooling) (Bierwirth et al., 2009). The second phase of SAMUM-1 was conducted in 2008 (SAMUM-2) on the Cape Verde Islands (Ansmann et al., 2011). One of the goals of the radiation measurements during SAMUM-2 was to determine the solar radiative forcing at the TOA over sea and for surface albedo values lower than 0.1.

A further goal of SAMUM-2 was to investigate Saharan dust after transport off the source region. Outbreaks of Saharan dust from the African continent towards the West frequently lead

\*Corresponding author.

e-mail: s.bauer@uni-leipzig.de

†Now at: European Southern Observatory (ESO), Garching, Germany.

DOI: 10.1111/j.1600-0889.2011.00567.x

to high concentrations of dust aerosol over the Atlantic Ocean (Prospero and Carlson, 1972). Close to the source region mostly pure dust is found, but after a long range transport the aging of the dust and mixing with other aerosol types modify the optical properties of the dust layers.

During SAMUM-2 mixing of biomass-burning smoke and Saharan dust were frequently observed (Ansmann et al., 2011). In this paper the influence of dust and biomass-burning smoke on the radiation budget of the atmosphere is studied at wavelength ranges in the visible and near infrared (0.4–2  $\mu\text{m}$ ). Due to the homogeneous surface albedo of the Atlantic Ocean the variability of upward radiation was mainly determined by the aerosol properties. To describe these aerosols, aerosol radiative properties were derived from measurements of upward spectral irradiances, radiances and particle extinction coefficients by a High Spectral Resolution Lidar (HSRL, Esselborn et al., 2009). The combinations of the collocated measurements of particle extinctions coefficients and irradiances allowed to derive conclusions on the chemical composition of the aerosol layers.

Two methods are compared for determining the average aerosol chemical compositions averaged over a vertical atmospheric column. In a first model-based method the optical properties of aerosol particles (single scattering albedo and asymmetry parameter) are retrieved from a combination of measurements and radiative transfer calculations. It is shown that the retrieved properties are uncertain to a high degree. Nevertheless, they are used for estimating the aerosol solar radiative forcing at the TOA. The derived radiative forcings along the flight tracks at the TOA are plotted as a function of aerosol optical depth. The slope of this plot gives the aerosol solar radiative forcing efficiency. It turns out that this quantity is closely linked to the aerosol chemical composition. Similar retrievals of aerosol optical properties were reported by Bergstrom et al. (2010) and Schmidt et al. (2010). In a second mostly measurement-based method similar to Redemann et al. (2006), the net irradiance (measured upward irradiance minus modelled downward irradiance) is plotted as a function of the aerosol optical depth and the resulting slope of the regression determines the forcing efficiency. The second method has the advantage that basically no model results are needed except for the downward irradiance which is less problematical due to low aerosol concentrations above the flight altitude.

In Section 2 basic definitions are introduced. An overview of the measurement flights performed during SAMUM-2 and information of aerosol layers from LIDAR measurements and backward trajectories are given in Section 3. Section 4 deals with the radiative transfer model used and the necessary input parameters for the calculations. The mainly model-based method is introduced in Section 5. The retrieval of the single scattering albedo and asymmetry parameter are explained in Section 5.1, the calculated aerosol solar radiative forcing at the TOA are represented in Section 5.2 and the determination of the aerosol solar radiative forcing efficiency is shown in Section 5.3. Section 6

deals with the net irradiance (measurement-based method) and the derived instantaneous aerosol solar radiative forcing efficiency. Conclusions with regard to the chemical composition of the aerosol particles are given in Section 7.

## 2. Definitions

Airborne upward spectral irradiance ( $F_\lambda^\uparrow$ ) was measured and used to derive the aerosol radiative forcing at the TOA, which is the difference between the net irradiance for the cases without aerosol (subscript ‘0’) and with aerosol (subscript ‘a’) in the atmosphere.

$$\Delta F_\lambda = (F_\lambda^\downarrow - F_\lambda^\uparrow)_a - (F_\lambda^\downarrow - F_\lambda^\uparrow)_0, \quad (1)$$

with  $F_\lambda^\downarrow$  representing the downward spectral irradiance. Following Redemann et al. (2006) the variation of the solar zenith angle is taken into account and the relative aerosol radiative forcing is calculated by

$$\Delta F_{\lambda,\text{rel}} = \frac{(F_\lambda^\downarrow - F_\lambda^\uparrow)_a - (F_\lambda^\downarrow - F_\lambda^\uparrow)_0}{F_\lambda^\downarrow}. \quad (2)$$

The spectral surface albedo is defined as the ratio of upward and downward irradiances.

$$\rho_\lambda = \frac{F_\lambda^\uparrow}{F_\lambda^\downarrow}. \quad (3)$$

The aerosol optical depth ( $\tau$ ) is calculated from the vertical integration of the particle extinction coefficient ( $b_{\text{ext}}$ ) profile:

$$\tau(z) = \int_z^\infty b_{\text{ext}}(z') dz'. \quad (4)$$

The radiative properties of aerosol particles are described by the single scattering albedo  $\omega$  and the asymmetry parameter  $g$ . The particle single scattering albedo  $\omega$  is defined as

$$\omega = \frac{b_{\text{sca}}}{b_{\text{ext}}} = \frac{b_{\text{sca}}}{b_{\text{sca}} + b_{\text{abs}}}, \quad (5)$$

with  $b_{\text{sca}}$  the volume scattering coefficient and  $b_{\text{abs}}$  the volume absorption coefficient of the particles. The particle single scattering albedo is a measure for the absorption of the aerosol particles. The asymmetry parameter  $g$  is defined as

$$g = \frac{1}{2} \int_{-1}^1 \cos \vartheta P(\cos \vartheta) d \cos \vartheta, \quad (6)$$

with the scattering angle  $\vartheta$  and the phase function  $P(\cos \vartheta)$ . The phase function describes the probability that photons are scattered in direction  $\vartheta$  measured from the direction of forward scattering (0 degrees).

The relative radiative forcing efficiency  $\Delta F_{\lambda,\text{eff,rel}}$  can be derived from the regression between the relative aerosol radiative forcing  $\Delta F_{\lambda,\text{rel}}$  and  $\tau$ . The slope represents the relative radiative forcing efficiency and it's a normalized (with respect to  $\tau$ ) measure of the radiative effects of the aerosol particles. It is

calculated by

$$\Delta F_{\lambda,\text{eff,rel}} = \frac{d(\Delta F_{\lambda,\text{rel}})}{d\tau} \quad (7)$$

Instead of the aerosol relative radiative forcing the relative net irradiance  $F_{\lambda,\text{net,rel}}$  with

$$F_{\lambda,\text{net,rel}} = \frac{F_{\lambda}^{\downarrow} - F_{\lambda}^{\uparrow}}{F_{\lambda}^{\downarrow}} \quad (8)$$

can be used in eq. (7) to calculate the instantaneous relative aerosol radiative forcing efficiency  $\Delta F_{\lambda,\text{eff,inst}}$ .

$$\Delta F_{\lambda,\text{eff,inst}} = \frac{dF_{\lambda,\text{net,rel}}}{d\tau} \quad (9)$$

### 3. Overview of measurements

SAMUM-2 was based in Praia on the Cape Verde Islands in January and February 2008. Praia is about 650 km west of the African mainland (Senegal) at 15° northern latitude (Ansmann et al., 2011). During the campaign, nine flights were conducted with the research airplane Falcon from the German Aerospace Center (DLR). These flights were carried out over the Atlantic Ocean at different altitudes (below, in and above aerosol layers). Upward spectral irradiance and radiance were measured with the Modular Airborne Spectral Radiation Measurement System (SMART) Albedometer in the wavelength range of 400–2000 nm. In this paper we just analyse the irradiance measurements. The SMART Albedometer (Wendisch et al., 2001) consists of optical inlets, optical fibre and a system of spectrometers. The spectrometers split the radiation into individual wavelengths (resolution of 2–3 nm in the visible and 9–16 nm in the near infrared), which are transmitted to a photo diode detector. The radiation measurements were calibrated with a standard 1000 W lamp and changes between the flight were corrected by transfer calibrations with an integrating sphere before each flight (Bierwirth et al., 2009). The optical inlets have been installed on the aircraft such that the orientation of the sensor was vertically downwards during the flight. The average temporal resolution during the flights was 3 s. Meteorological vertical profiles of air temperature, pressure and humidity were measured at selected way points with dropsondes. Furthermore, airborne measurements by an HSRL (Esselborn et al., 2009) were available from the aircraft, which retrieved vertical profiles of volume extinction coefficients  $b_{\text{ext}}$  below the aircraft at a wavelength of 532 nm and a time resolution of about 2 s. Additionally, columnar values of  $\tau$  from the ground-based sun photometer (Toledano et al., 2011) in Praia at a wavelength of 1030 nm were available.

An overview of the flights is given in Table 1. The meteorological synoptic conditions during SAMUM-2, the resulting air mass advection from areas of different aerosol-type sources and the evolution of the layering are described in Knippertz et al. (2011). During SAMUM-2 three phases can be distinguished:

Table 1. Overview of the nine flights during SAMUM-2

Date	Flight track
22 Jan 2008	Southeast from Cape Verde over the Atlantic ocean
23 Jan 2008	Southeast from Cape Verde over the Atlantic ocean
25 Jan 2008	Overflights Praia (Cape Verde)
28 Jan 2008	Cape Verde - Canary Islands
29 Jan 2008	Cape Verde - Senegal
30 Jan 2008	Northwest from Cape Verde over the Atlantic ocean
04 Feb 2008	Southeast from Cape Verde over the Atlantic ocean
05 Feb 2008	Cape Verde - Senegal
06 Feb 2008	Overflights Praia (Cape Verde)

(i) 21–26 January: Pure dust at lower altitudes up to around 1.5 km and layers with a mixing of dust and biomass-burning smoke at higher altitudes (up to around 5 km).

(ii) 27–30 January: Mostly pure dust at lower altitudes (with less maritime components on 28 January) and no mixing with biomass-burning smoke at higher altitudes.

(iii) 31 January–5 February: Dust plus maritime aerosol at lower altitudes and mixing of dust and biomass-burning smoke at higher altitudes.

To derive the aerosol components from the SMART measurements of upward irradiances several flight intervals were selected where the airplane flew over the aerosol layers and no clouds were observed. Two exemplary cases are presented in this paper in detail. The first case is from a flight conducted on 22 January (13:25 to 13:35 UTC) with a mixing of Saharan dust and biomass-burning smoke (in the following referred as biomass case). The second case results from a flight on 28 January (16:00 to 16:15 UTC) with pure dust (in the following referred as pure dust case). The flight tracks on these days are given in Fig. 1. During the biomass case the flight track is to the southeast and the flight altitude was higher than 8 km and above all aerosol layers. The distance covered was 90 km (in about 10 min). During the pure dust case a distance of 172 km (covered in a time of 15 min) was selected and the flight altitude was higher than 8 km. Figure 2 shows the 72 h backward trajectories at 500 and 3000 m height for the Cape Verde Islands for the two cases. In both the cases the 500 m trajectory came from eastern direction, that is, from Saharan region with dust aerosol particles. This is consistent with Fig. 1a in (Knippertz et al., 2011, 22 and 28 day of year). Additionally, the 3000 m trajectory for the biomass case shows air mass advection from the southeast which means from the inflow area of biomass-burning smoke from the southern West Africa. This can also be seen in Fig. 1a in (Knippertz et al., 2011, 22 day of year), where the higher aerosol layers consist of dust and biomass-burning smoke. The 3000 m trajectory for the pure dust case is not from areas with biomass-burning smoke and dust, in accordance with (Knippertz et al., 2011, 28 day of year), where no aerosol

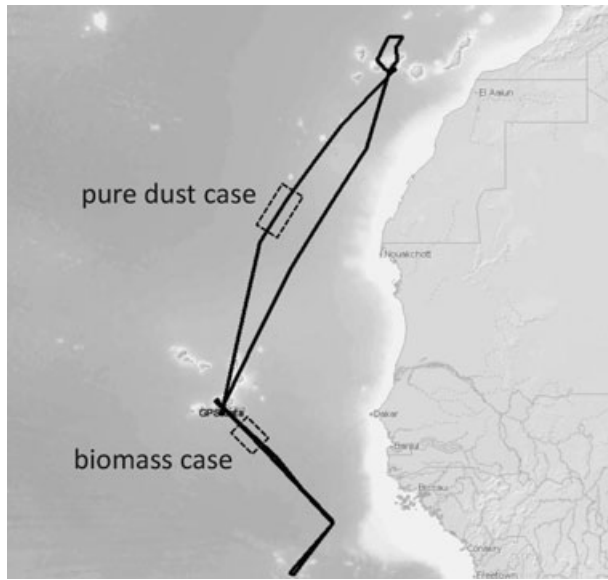


Fig. 1. Flight tracks and selected intervals (dashed rectangle) for determining the relative aerosol solar radiative forcing efficiency at the top of atmosphere and the aerosol solar net radiative forcing efficiency at flight altitude on 22 January (biomass case) and 28 January (pure dust case). [Plot created with GPS Visualizer (gpsvisualizer.com).]

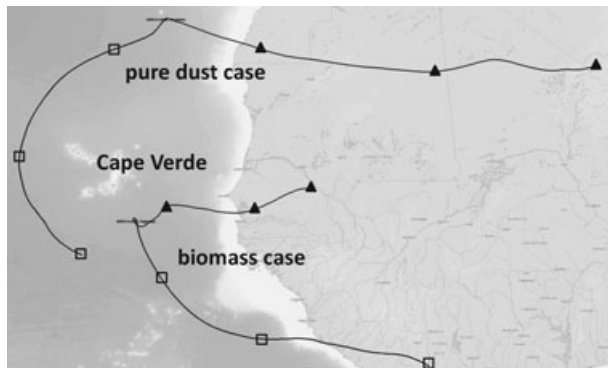


Fig. 2. 72 h HYSPLIT backward trajectories (Draxler and Rolph 2010, <http://ready.arl.noaa.gov/HYSPLIT.php>) for the pure dust and biomass case. The trajectories with the full triangles are the 500 m trajectories above sea level, the open squares mark the 3000 m trajectories. (plot created with GPS Visualizer(gpsvisualizer.com))

particles were observed. Among the selected intervals, the aircraft flew at some distance from Cape Verde. However, a comparison of the determined backward trajectories during the selected periods for the Cape Verde and corresponding aircraft position show the same origin of air masses.

#### 4. Radiative transfer model

For the simulation of the spectral irradiance, the software package libradtran (Mayer and Kylling, 2005) was applied. The DISORT 2 radiative transfer scheme by Stamnes et al.

(1988) was selected and as gas absorption parametrization, SBDART/LOWTRAN by Ricchiazzi et al. (1998) was applied. As input the measured profiles of air pressure, temperature and trace gases concentrations were implemented from dropsonde measurements in accordance with the U.S. Standard atmosphere (Anderson et al., 1986). Vertical profiles of spectral particle extinction coefficients (measured by the HSRL), single scattering albedo and asymmetry parameter were included. To obtain spectra of particle optical depth the Ångström coefficients ( $\alpha$  and  $\beta$ ) were calculated from

$$\tau(\lambda_1) = \beta \cdot \lambda_1^{-\alpha} = \tau(\lambda_2) \cdot \lambda_1^{-\alpha}. \quad (10)$$

$\beta$  was determined from the extinction coefficients of the airborne HSRL and  $\alpha$  from the sun photometer on Cape Verde.

Another important parameter for the radiative transfer simulations of upward irradiances is the surface albedo, which was determined from upward irradiance measured during low level flights applying an algorithm by Wendisch et al. (2004).

#### 5. Retrieval results

##### 5.1. Particle single scattering albedo and asymmetry parameter

The optical properties of aerosol particles are described in the radiative transfer model by the aerosol optical depth  $\tau$ , which is available from the HSRL measurements, the single scattering albedo  $\omega$  and the asymmetry parameter  $g$ .  $\omega$  and  $g$  were not measured during the flights and, therefore, we have assumed different combinations of both parameters as input for the radiative transfer model. The combination which yields a minimum deviation between the measured and calculated upward irradiances gives the most reasonable values of  $\omega$  and  $g$ . Therefore, simulations of the upward irradiances with a set of combinations of  $\omega$  and  $g$  (both in the range from 0 to 1 with a resolution of 0.05) were compared with the upward irradiance measurements. For each combination of  $\omega$  and  $g$  the mean square deviation between simulation and measurement was calculated. Figure 3 shows an example for a retrieval result for the biomass case for a wavelength of 532 nm. On the left plot the mean square deviation of the whole range of  $\omega$  from 0 to 1 and  $g$  from 0 to 0.67 is shown (higher  $g$  are not plotted, because pre-calculations showed no significant gradient to other minima higher than 0.67). The black spots in Fig. 3 present the local minima of the mean square deviation, which are within the measurement uncertainty. Several local minima are obvious within a range of about 0.1 of  $g$  (between 0.6 and 0.67) and  $\omega$  (between 0.95 and 1) indicating ambiguous solutions of the iteration. The right-hand plot of Fig. 3 shows the same results as the left-hand one but in a reduced range. A selection of the minima of the mean square deviation at 532 nm wavelength for the biomass case and pure dust case is shown in Table 2. Figure 4 shows spectra of  $\omega$  and  $g$  for the biomass case. To determine the uncertainty of

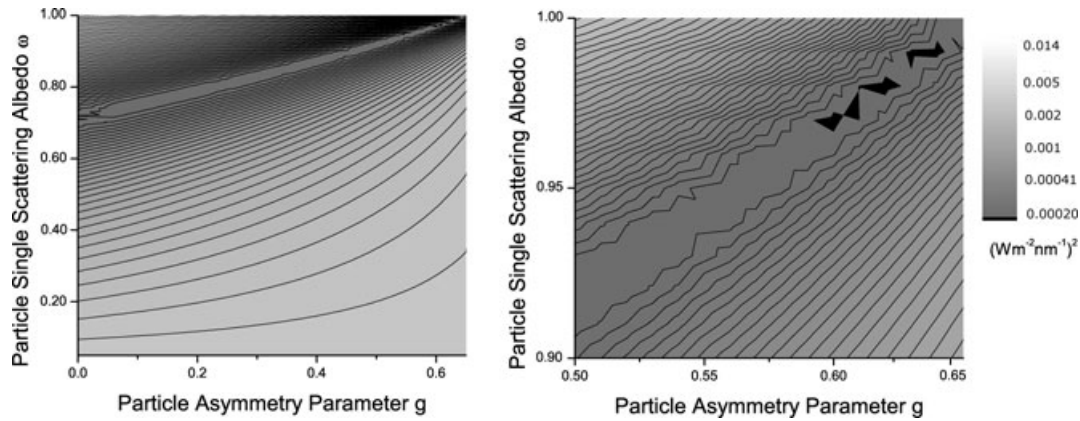


Fig. 3. Mean square deviation (shades of grey in the contour plot) between calculation and measurement of the upward irradiance at different combinations of the single scattering albedo  $\omega$  and the asymmetry parameter  $g$  for the biomass case for a wavelength of 532 nm. The black spots present the minimal differences between calculation and measurement. The left-hand plot shows the calculated mean square deviation for  $\omega$  from 0 to 1 and  $g$  from 0 to 0.67 (pre calculation for  $g$  higher than 0.67 showed no gradients to other minima.) The right-hand plot shows the enlarged section of the left-hand plot around the minima.

Table 2. Selection of determined asymmetry parameter  $g$  and the single scattering albedo  $\omega$  at a wavelength of 532 nm for different times

Time/h (UTC)	$g$	$\omega$
Biomass case (22 January 2008)		
13:25	0.62	0.97
13:30	0.63	0.97
13:35	0.65	0.96
Pure dust case (28 January 2008)		
16:00	0.59	0.92
16:05	0.54	0.90
16:10	0.63	0.93
16:15	0.65	0.90

the two parameters the retrieval was additionally conducted for the maximum measurement errors of the upward irradiances. This results in uncertainties of 8% for  $\omega$  and 10% for  $g$ , and are shown in Fig. 4, where an example for the spectral variability of  $\omega$  and  $g$  is plotted. The retrieval of particle single scattering albedo and asymmetry parameter was done for several flights with a temporal resolution of about 1 min and it showed that the uncertainty is large.

## 5.2. Aerosol solar radiative forcing

The upper plot in Fig. 5 shows the time series of calculated broad-band relative aerosol solar radiative forcing at the TOA and  $\tau$  at 532 nm for the biomass case. It is always negative, that is, in the solar wavelength range the aerosol results in a cooling of the atmosphere. There is also a close correlation

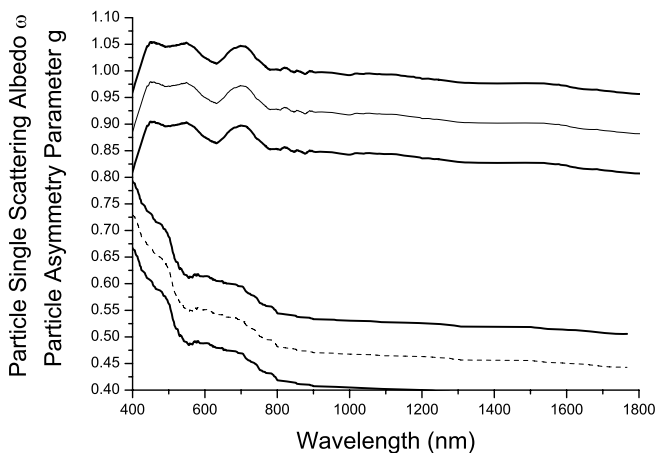


Fig. 4. Wavelength dependence of the single scattering albedo  $\omega$  [solid plot (non bold)] and asymmetry parameter  $g$  (dashed plot) on 22 January 2008, 13:30 UTC. The bold line above and below the  $\omega$  and  $g$  spectra represent the uncertainties.

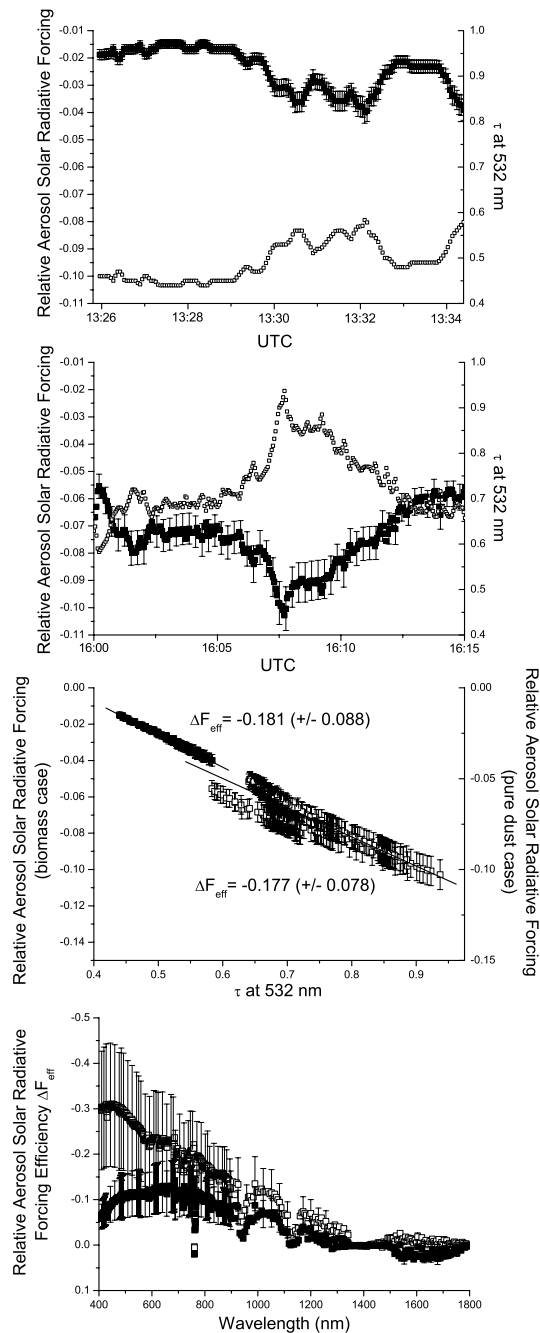


Fig. 5. These plots represent the derivation of the relative aerosol solar radiative forcing efficiency with the method of retrieving the  $\omega$  and  $g$ . The upper plot shows the temporal variation of the broad-band relative aerosol solar radiative forcing (left, y-axis/full squares) and  $\tau$  (right, x-axis and open squares) for the biomass case, the second one for the pure dust case. The third plot shows the broad-band relative aerosol solar radiative forcing versus  $\tau$  at 532 nm for the biomass case (full squares), the pure dust case (open squares) and the resulting relative aerosol solar radiative forcing efficiency  $\Delta F_{\text{eff,rel}}$ . The spectral relative aerosol solar radiative forcing efficiencies are shown in the bottom plot for the biomass case (full squares) and the pure dust case (open squares).

between the relative aerosol solar radiative forcing and  $\tau$ . A minimum of  $\tau$  coincides with a maximum of the relative aerosol solar radiative forcing. This means that low values of  $\tau$  lead to a smaller magnitude of radiative forcing and to less cooling, respectively. The variability of the relative aerosol solar radiative forcing depends on the particle single scattering albedo, particle asymmetry parameter and primarily on the change of  $\tau$ . The same correlation of  $\tau$  and radiative forcing and with respect to cooling effect can be seen for the pure dust case (second plot of Fig. 5). The relative aerosol solar radiative forcing of the biomass case is higher than of the dust case. The reason can be the higher aerosol optical depth or/and the higher single scattering albedo (Table 2). Therefore, a direct comparison of both cases with respect to the aerosol types without the aerosol solar radiative forcing efficiency is not possible.

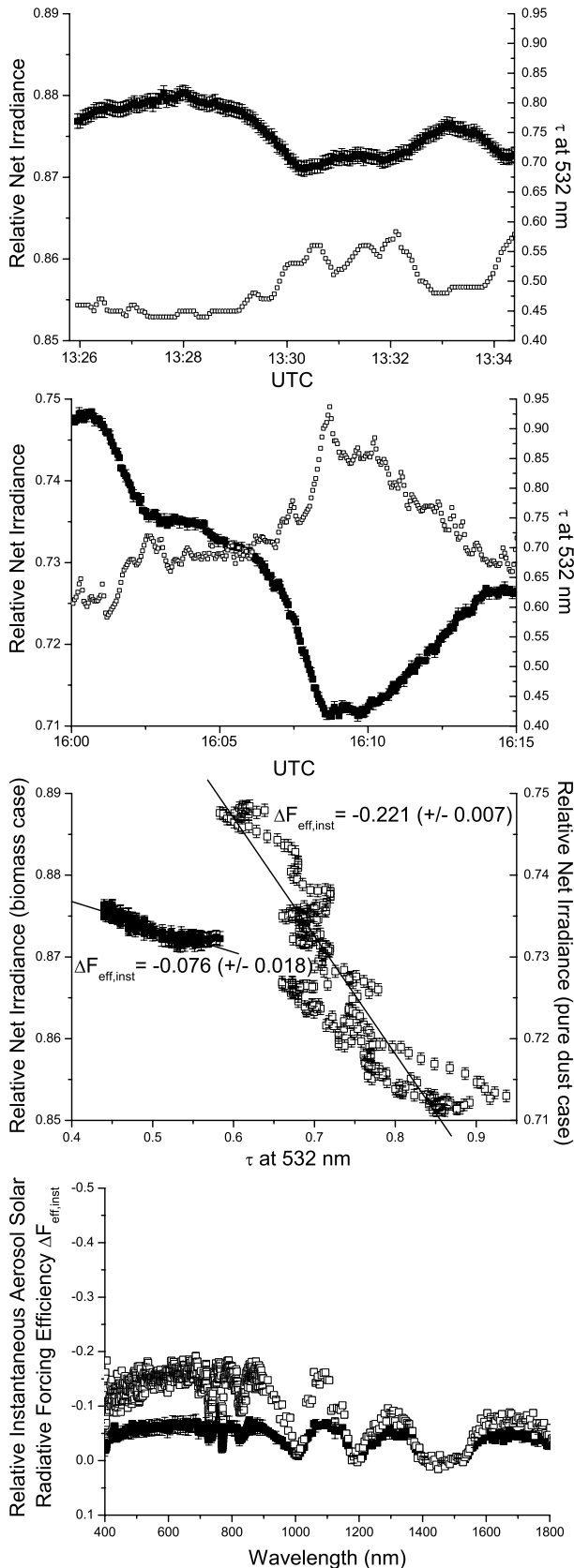
### 5.3. Aerosol solar radiative forcing efficiency

The relative aerosol solar radiative forcing efficiency (eq. 7) depends on the radiative properties of aerosol particles. For example, soot aerosol particles from combustion processes have a lower single scattering albedo than Saharan dust due to their higher absorption and, therefore, a higher relative aerosol solar radiative forcing efficiency. This means with increasing  $\tau$  absorbing aerosol particle lead to less cooling or even higher warming effects.

The third plot of Fig. 5 shows the broad-band relative aerosol solar radiative forcing versus the  $\tau$  for the biomass case and the pure dust case. It shows clearly a linear trend for both cases with a higher magnitude of the slope of  $-0.181 (\pm 0.088)$  for the biomass case, which represents the relative aerosol solar radiative forcing efficiency, than for the pure dust case [slope of  $-0.177 (\pm 0.078)$ ]. An opposite trend was expected, because more absorbing aerosol particles in the biomass case leads to less relative aerosol solar radiative forcing efficiency. However, uncertainties are large and, therefore, no differences in the composition of dust can be derived from this method.

The left-hand plot in Fig. 7 gives an overview of the relative aerosol solar radiative forcing efficiencies for the biomass case (column 1), an additional biomass case on 23 January (column 2) and the pure dust case (column 3). Considering the uncertainties (vertical bars) there are no differences between the three cases. Due to the high uncertainties in determining  $\omega$  and  $g$  expected differences of the forcing efficiencies during these days are not obvious. This method is not convenient for determining aerosol types only with measured upward irradiances.

Beside the determination of the broad-band relative aerosol solar radiative forcing versus the measured  $\tau$  at 532 nm, the spectral relative aerosol solar radiative forcing versus the respective spectral  $\tau$  (from Ångström coefficients) were used to calculate the spectral relative aerosol solar radiative forcing efficiencies. The result is shown in the bottom plot of Fig. 5 for the biomass and pure dust case. Considering the uncertainties,



only for lower wavelengths up to 500 nm the efficiencies for the biomass case is higher in magnitude than for the pure dust case. Else there are no differences between both cases as for the broad-band efficiencies shown in the left-hand plot of Fig. 7.

## 6. Measurement-based, instantaneous aerosol radiative forcing

Section 5 describes the model-based determination of the aerosol solar radiative forcing from the retrieved values of  $\omega$  and  $g$ . The retrieval of  $\omega$  and  $g$  has large uncertainties. To avoid this problem an alternative, mostly measurement-based method to estimate the aerosol solar radiative forcing is applied in this section. For this purpose the relative net irradiance (eq. 8) is used. This method, as described by Redemann et al. (2006), which does not use modelled downward irradiances in contrast to this paper, only requires the measurements of the upward irradiance and the modelling of the downward irradiance at the flight altitude. Thus, a minimum in the aerosol optical depth leads to a maximum in the relative net irradiance and vice versa. This correlation is shown for the considered biomass case (upper plot in Fig. 6) and the pure dust case (second plot in Fig. 6) for the broad-band relative net irradiance. The uncertainty of the relative net irradiance is small (lower than 1%) in contrast to the calculated relative aerosol solar radiative forcing on the base of the retrieved aerosol optical properties. The uncertainty is determined by calculating the relative net irradiance using the maximum errors of the measured upward irradiances. To determine the relative instantaneous aerosol solar radiative forcing efficiency (eq. 9) for the biomass and the pure dust case the relative net irradiance was plotted versus  $\tau$  (third plot in Fig. 6). The plots show a linear trend for the fixed period and the plotted linear regression, which represents the instantaneous relative aerosol solar radiative forcing efficiency, has a slope of  $-0.076$  with an uncertainty of  $0.018$  for the biomass case and  $-0.221$  (uncertainty  $\pm 0.007$ ) for the pure dust case. These differences can be observed for several other cases. An overview of the determined relative instantaneous aerosol solar radiative forcing efficiencies is shown in Fig. 7 (right-hand plot) for the biomass case

Fig. 6. These plots represent the derivation of the relative aerosol solar radiative forcing efficiency with the method calculating the net irradiance. The upper plot shows the temporal variation of the broad-band relative net irradiance (left, y-axis/full squares) and  $\tau$  (right, x-axis and open squares) for the biomass case, the second one for the pure dust case. The third plot shows the broad-band relative net irradiance versus  $\tau$  at 532 nm for the biomass case (full squares), the pure dust case (open squares) and the resulting relative instantaneous aerosol solar radiative forcing efficiency  $\Delta F_{\text{eff,inst}}$ . The spectral relative aerosol solar radiative forcing efficiencies are shown in the bottom plot for the biomass case (full squares) and the pure dust case (open squares).

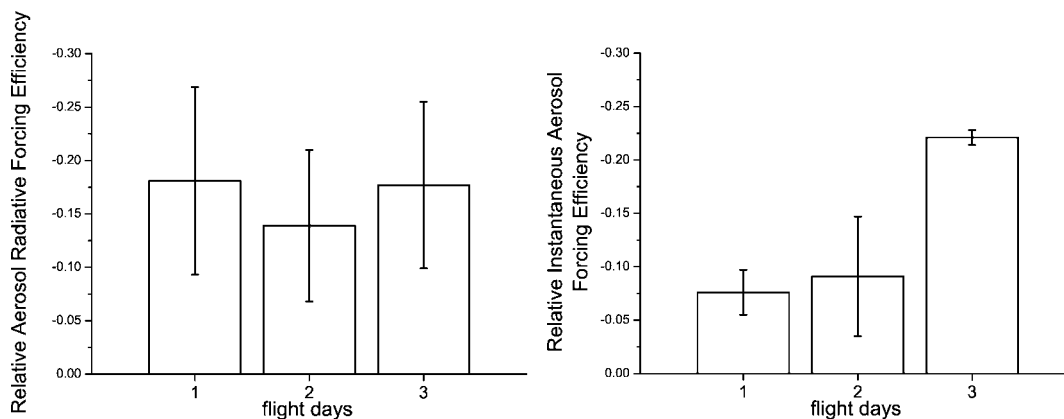


Fig. 7. Overview of the broad-band relative aerosol solar radiative forcing efficiency (left-hand plot, y-axis) and the broad-band relative instantaneous aerosol solar radiative forcing efficiency for three flight intervals (x-axis): 1 = 22 January (biomass case), 2 = 23 January (biomass case) and 3 = 28 January (pure dust case).

(column 1), an additional biomass case on 23 January (column 2) and the pure dust case (column 3). In spite of the uncertainties the two biomass cases have clearly lower relative instantaneous aerosol solar radiative forcing efficiencies in magnitude than the pure dust case. This was expected because biomass-burning smoke leads to more absorbing and therefore to less cooling per unit  $\tau$ . The same clear differences are shown in bottom plot of Fig. 6 for the spectral instantaneous relative aerosol solar radiative forcing efficiencies. At most wavelengths, except the absorption bands, where no irradiances were measured and forcing efficiencies are 0, the forcing efficiencies of the biomass case are higher in magnitude than for the pure dust case.

## 7. Summary and conclusion

In January and February 2008, airborne measurements of upward spectral irradiances in a wavelength range of 400–2000 nm were performed during the SAMUM-2 campaign. Together with concurrent vertical profile measurements of particle extinction coefficients from an HSRL in combination with ground-based sun photometer measurements spectral aerosol optical thickness were determined along the flight tracks. The spectral albedo for flights over water were determined from the measured upward irradiances applying an iteration technique by Wendisch et al. (2004). Particle single scattering albedo and asymmetry parameter were retrieved and from these parameters the relative aerosol solar radiative forcing was determined at the TOA. The change of the relative aerosol solar radiative forcing per unit  $\tau$  is a measure for the absorbing properties of aerosol particles. High uncertainties are inherent in the retrieval of  $\omega$  and  $g$  by this method; it introduces unacceptable uncertainties into the calculation of aerosol solar radiative forcing. Another, mostly measurement-based method was presented which uses, instead of the relative aerosol solar radiative forcing, the relative net irradiance. It is shown that the change of the relative net irra-

diance (instantaneous relative aerosol solar forcing efficiency) with increasing  $\tau$  is related to the aerosol chemical composition. Aerosol layers with a fraction of biomass-burning smoke revealed an instantaneous relative aerosol solar forcing efficiency of  $-0.076$  (uncertainty of 0.018) and pure dust  $-0.221$  (uncertainty of 0.007). The magnitudes of instantaneous relative forcing efficiency is lower with an increasing fraction of absorbing aerosol particles like biomass-burning smoke.

## 8. Acknowledgments

This study and the SAMUM research group are funded by the Deutsche Forschungsgemeinschaft (DFG), contract FOR 539.

## References

- Anderson, G., Clough, S., Kneizys, F., Chetwynd, J. and Shettle, E. 1986. AFGL atmospheric constituent profiles (0–120 km), Technical Report AFGL-TR-86-0110, AFGL (OPI), Hanscom AFB, MA 01736.
- Ansmann, A., Petzold, A., Kandler, K., Tegen, I., Wendisch, M. and co-authors. 2011. Saharan Mineral Dust Experiments SAMUM-1 and SAMUM-2: what have we learned? *Tellus* **63B**, In press.
- Bergstrom, R. W., Schmidt, K. S., Coddington, O., Pilewskie, P., Guan, H. and co-authors. 2010. Aerosol spectral absorption in the Mexico City area: results from airborne measurements during MILAGRO/INTEX B. *Atmos. Chem. Phys.* **10**(13), 6333–6343. doi:10.5194/acp-10-6333-2010.
- Bierwirth, E., Wendisch, M., Ehrlich, A., Heese, B., Tesche, M. and co-authors. 2009. Spectral surface albedo over Morocco and its impact on the radiative forcing of Saharan dust. *Tellus* **61B**, 252–269.
- Chen, G., Ziemba, L. D., Chu, D. A., Thornhill, K. L., Schuster, G. L. and co-authors. 2010. Observations of Saharan dust microphysical and optical properties from the Eastern Atlantic during NAMMA airborne campaign. *Atmos. Chem. Phys.* **10**, 13445–13493.
- Esselborn, M., Wirth, M., Fix, A., Weinzierl, B., Rasp, K. and co-authors. 2009. Spatial distribution and optical properties of Saharan dust

- observed by airborne high spectral resolution lidar during SAMUM 2006. *Tellus* **61B**, 131–143.
- Formenti, P., Rajot, J. L., Desboeufs, K., Caquineau, S., Chevaillier, S. and co-authors. 2008. Regional variability of the composition of mineral dust from western Africa: results from the AMMA SOP0/DABEX and DODO field campaigns. *J. Geophys. Res.* **113**(D20). doi:10.1029/2008JD009903.
- Forster, P., Ramaswamy, V., Artaxo, P., Bernsten, T., Betts, R. and co-authors. 2007. *Changes in Atmospheric Constituents and in Radiative Forcing*, Cambridge University Press, Cambridge, UK and NY, USA.
- Heintzenberg, J. 2009. The SAMUM-1 experiment over Southern Morocco: overview and introduction. *Tellus* **61B**, 2–11.
- IPCC 2007. Climate Change 2007: The Physical Science Basis. Contributions of Working Group I to the Fourth Assessment Report of the Intergovernmental Panel on Climate Change. IPCC Cambridge University Press, UK.
- Johnson, B. T., Christopher, S., Haywood, J. M., Osborne, S. R., McFarlane, S. and co-authors. 2009. Measurements of aerosol properties from aircraft, satellite and ground-based remote sensing: a case-study from the Dust and Biomass-burning Experiment (DABEX). *Quart. J. R. Meteorol. Soc.* **135**(641), 922–934. doi:10.1002/qj.420.
- Knippertz, P., Tesche, M., Heinold, B., Kandler, K., Toledano, C. and co-authors. 2011. Dust mobilization and aerosol transport from West Africa to Cape Verde: a meteorological overview of SAMUM-2. *Tellus* **63B**, In press.
- Lyamani, H., Olmo, F., Alcántara, A. and Alados-Arboledas, L. 2006. Atmospheric aerosols during the 2003 heat wave in southeastern Spain II: microphysical columnar properties and radiative forcing. *Atmos. Env.* **40**, 6465–6476.
- Mayer, B. and Kylling, A. 2005. Technical note: the libRadtran software package for radiative transfer calculations, description and examples of use. *Atmos. Chem. Phys.* **5**, 1855–1877.
- Meloni, D., Di Sarra, A., Pace, G. and Monteleone, F. 2006. Aerosol optical properties at Lampedusa (Central Mediterranean), 2. Determination of single scattering albedo at two wavelengths for different aerosol types. *Atmos. Chem. Phys.* **6**, 715–727.
- Prospero, J. M. and Carlson, T. N. 1972. Vertical and areal distribution of Saharan dust over western equatorial North-Atlantic Ocean. *J. Geophys. Res.* **77**(27), 5255.
- Redemann, J., Pilewskie, P., Russell, P. B., Livingston, J. M., Howard, S. and co-authors. 2006. Airborne measurements of spectral direct aerosol radiative forcing in the Intercontinental chemical Transport Experiment/Intercontinental Transport and Chemical Transformation of anthropogenic pollution, 2004. *J. Geophys. Res.* **111**(D14). doi:10.1029/2005JD006812.
- Ricchiazzi, P., Yang, S., Gautier, C. and Sowle, D. 1998. SBDART: A research and teaching software tool for plane-parallel radiative transfer in the Earth's atmosphere. *Bull. Amer. Meteorol. Soc.* **79**, 2101–2114.
- Schmidt, K. S., Pilewskie, P., Bergstrom, R., Coddington, O., Redemann, J. and co-authors. 2010. A new method for deriving aerosol solar radiative forcing and its first application within MILAGRO/INTEX-B. *Atmos. Chem. Phys.* **10**(16), 7829–7843. doi:10.5194/acp-10-7829-2010.
- Shell, K. and Somerville, R. 2007. Sensitivity of climate forcing and response to dust optical properties in an idealized model. *J. Geophys. Res.* **112**, doi:10.1029/2006JD007198.
- Stamnes, K., Tsay, S., Wiscombe, W. and Jayaweera, K. 1988. A numerically stable algorithm for discrete-ordinate-method radiative transfer in multiple scattering and emitting layered media. *Appl. Opt.* **27**(12), 2502–2509.
- Tanre, D., Haywood, J., Pelon, J., Leon, J. F., Chatenet, B. and co-authors. 2003. Measurement and modeling of the Saharan dust radiative impact: overview of the Saharan Dust Experiment (SHADE). *J. Geophys. Res.* **108**(D18). doi:10.1029/2002JD003273.
- Toledano, C., Wiegner, M., Gro, S., Freudenthaler, V., Gasteiger, J. and co-authors. 2011. Optical properties of aerosol mixtures derived from sun-sky radiometry during SAMUM-2. *Tellus* **63B**, In press.
- Wang, S.-H., Lin, N.-H., Chou, M.-D. and Woo, J.-H. 2007. Estimate of radiative forcing of Asian biomass-burning aerosols during the period of TRACE-P. *Atmos. Chem. Phys.* **112**(D10). doi:10.1029/2006JD007564.
- Wendisch, M., Müller, D., Schell, D. and Heintzenberg, J. 2001. An airborne spectral albedometer with active horizontal stabilization. *J. Atmos. Oceanic Technol.* **18**(11), 1856–1866.
- Wendisch, M., Pilewskie, P., Jäkel, E., Schmidt, S., Pommier, J. and co-authors. 2004. Airborne measurements of areal spectral surface albedo over different sea and land surfaces. *J. Geophys. Res.* **109**(D8), Art. No. D08203.